Reconfigurable band alignment of m-GaS/n-XTe$_2$ (X = Mo, W) multilayer van der Waals heterostructures for photoelectric applications

Xueping Li,[1,2] Ting Liu,[2] Lin Li,[2] Mengjie He,[2] Chenhai Shen,[2] Jingbo Li,[3] and Congxin Xia[2,*]

[1]*College of Electronic and Electrical Engineering, Henan Normal University, Xinxiang, Henan 453007, China*

[2]*School of Physics, Henan Normal University, Xinxiang 453007, China*

[3]*Institute of Semiconductors, South China Normal University, Guangzhou 510631, China*

(Received 16 May 2022; revised 10 August 2022; accepted 2 September 2022; published 19 September 2022)

Integrating two-dimensional materials into van der Waals heterostructures (vdWHs) is considered to be an efficient strategy for multifunctional devices. Here, the m-GaS/n-MoTe$_2$ (WTe$_2$) multilayer vdWHs are designed to explore possible characteristics through engineering the electric field, strain, and layer combination *m/n*. For the most stable GaS/MoTe$_2$ (WTe$_2$) bilayer vdWHs obtained by global search with direct band structure and straddling gap, the proper compression strain and positive electric field regulates the band structure from straddling gap to staggered case. Particularly, the m-GaS/n-WTe$_2$ multilayer vdWHs have the straddling band alignment when the layer number of GaS is 1L ($m = 1$), while it can be transferred to staggered case with the $m > 1$ due to the quantum confinement effect. In addition, the GaS/MoTe$_2$ vdWHs can be used as highly efficient solar cells with power conversion efficiency up to 27%. Also, the photoresponsivity and external quantum effects are increased from 0.048 (8%) to 0.18 A/W (42%) for the multilayer vdWHs. These results indicate that the m-GaS/n-MoTe$_2$ (WTe$_2$) multilayer vdWHs can be taken as reconfigurable system in highly efficient solar cells and photodetectors.

DOI: 10.1103/PhysRevB.106.125306

I. INTRODUCTION

Recently, two-dimensional (2D) materials were discovered to possess novel characteristics in electronic and optical performances as well as promising use in technological devices [1–6]. However, the single 2D materials have their own shortcoming, which can greatly restrict the potential application. Thus, the performance of these materials usually requires to be modified or broadened through some modulation methods, in which combing with different 2D materials to build van der Waals heterostructures (vdWHs) is taken as available strategy [7–10]. For instance, the graphene/GaAs and MoSSe/Te vdWHs can realize high-efficiency solar cells with power conversion efficiency (PCE) to 16.2 and 22.6%, respectively [11,12]. Also, the PCE of HfN$_2$/MoTe$_2$ vdWHs can reach 21.44% due to the small conduction-band offset [13]. In addition, the SnSe/InSe vdWHs demonstrate excellent performance in photodetectors with detectivity up to 5.8×10^{10} Jones [14]. The previous studies obviously indicate that the vdWHs exhibit better performance in photodetector and solar cells than that of corresponding monolayers.

The group-III monochalcogenides have enormous application talent in optoelectronics due to suitable band gap, high carrier mobility, and nonlinear optical properties, especially for the GaS [15–20]. It is reported that layered GaS has been experimentally synthesized by a variety of means, and the band-gap value is 3.3 eV, indicating its meaningful in photocatalysis and ultraviolet (UV) detectors [21–23]. The InS/GaS vdWHs are proved to have profound effect on photocatalysis due to suitable band edge [24]. Also, the GaS/GaSe vdWHs have formed staggered band alignment and ensured excitons physically separated, which is suitable for solar energy conversion [25]. Moreover, the UV photoelectric detectors with ultralow detection limit are prepared successfully based on GaS [26]. The experimental result shows that GaS monolayer has significant photoresponsivity (19.2 AW^{-1} at 254 nm) due to strong absorption between UV and visible region [27]. Recently, the photodetectors of high photoresponsivity and broad wavelengths have been realized in GaS/WS$_2$ vdWHs [28]. All these findings make GaS a potential candidate for high-performance photodetectors.

Here, we design the GaS/MoTe$_2$ (WTe$_2$) multilayer vdWHs and explore their potential performance. The transition-metal chalcogenides (TMDCs) are chosen because of their direct band structures and excellent mobility [29–32]. In addition, the recent successful synthesis in the experiment also gives more opportunities to construct the vdWHs based on TMDCs [33,34]. On the other hand, the electronic performance can be tuned through the strain, electric field, and vdWHs [35–38]. For instance, Klaus *et al.* investigated the exciton peak evolution with different biaxial strains, which explain the experiments on strain-adjustable spectra of TMDCs [39]. Staggered band alignment in WTe$_2$/As vdWHs with the strain of 2% can be achieved, which is beneficial for reducing the recombination of electron-hole pairs [40]. Considering better lattice mismatch between the GaS and XTe$_2$ (X = Mo, W) monolayers, and there are few studies on MoTe$_2$ (WTe$_2$)-based vdWHs, so we select MoTe$_2$ (WTe$_2$) as representative ones of TMDCs to construct the heterojunction with GaS

*xiacongxin@htu.edu.cn

 ©2022 American Physical Society

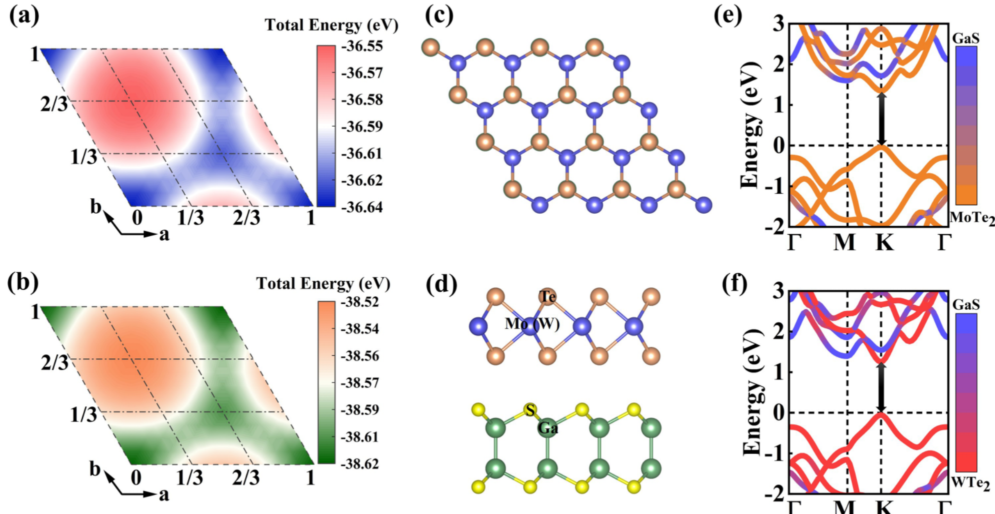

FIG. 1. Heat map of total energy vs in-plane shift for (a) GaS/$MoTe_2$ and (b) GaS/WTe_2 vdWHs, considering the 12×12 grid. (c) Top and (d) side view for the most stable configuration of GaS/$MoTe_2$ (WTe_2) vdWHs. Layer-dependent projected band structures for (e) GaS/$MoTe_2$ and (f) GaS/WTe_2 vdWHs.

and study the corresponding properties. Notably, the characteristics of 2D vdWHs can be obviously modulated by the layer combination through the experiment but it has not been systematically studied in the theory. We can forecast this m-GaS/n-$MoTe_2$ (WTe_2) multilayer vdWHs to possess newfangled performance. Thus, we construct m-GaS/n-$MoTe_2$ (WTe_2) multilayer vdWHs and systematically explored the structural, electronic properties, and relevant applications through engineering the electric field, strain, and layer combination, which opens up more possibilities for developing high-efficiency photodetector and solar cells.

II. METHODS

All the results are obtained by adopting the Vienna *Ab initio* Simulation Package (VASP) based on density-functional theory (DFT) [41–43], where the generalized gradient approximation of Perdew-Burke-Ernzerhof (PBE) is applied to express the electronic exchange and correlation [44,45], and the Heyd-Scuseria-Ernzerhof (HSE06) method is used to gain more precise band-gap value [46]. The electron-ion potential is simulated by projected augmented-wave potential [47]. Furthermore, vdW interaction in the GaS/$MoTe_2$ (WTe_2) multilayer vdWHs is corrected by DFT-D2 method [48,49]. The dipole correction is also taken into account in our calculations. Besides, the out-of-plane vacuum region larger than 20 Å is introduced, and the plane-wave cutoff is employed as 400 eV. The total convergent tolerance in energy and the forces on each atom converge are set to less than 10^{-5} eV and 0.01 eV/Å. A $15 \times 15 \times 1$ k-point mesh is adopted for the sampling in reciprocal space [50]. In addition, the electronic properties of monolayer GaS, $MoTe_2$, WTe_2, vdWHs and corresponding tuning of electric field and external strain are all stimulated by employing HSE06 methods. Note that to save computing resources, we only employ the PBE method to stimulate the electronic properties with the layer combination to obtain the variation trend. Moreover, we calculate the photocurrent density of the vdWHs based on the nonequilibrium Green function method at the PBE level, implemented in the QUANTUM ATK software [12,51]. The polarization direction of the light is parallel to the interface of GaS/$MoTe_2$ (WTe_2) vdWHs. To extend electron density, the Pseudo Dojo pseudopotential with medium basis set is used. We employ a density-mesh cutoff of 105 hartree and Monkhorst-Pack k mesh of $1 \times 13 \times 157$ for the transport characteristics simulations.

III. RESULTS AND DISCUSSION

A. Structure search and electronic properties of vdWHs

To build the reliable GaS/$MoTe_2$ (WTe_2) vdWHs, a global structure search method is performed for the 2D GaS/$MoTe_2$ (WTe_2) vdWHs with a 12×12 displacement grid, corresponding to 144 stacking structures $A_{m,n}$. The symbol $A_{m,n}$ means the displacement of the GaS layer relative to the $MoTe_2$ (WTe_2) layer is $(m/12)\vec{a} + (m/12)\vec{b}$, where $\vec{a}$ and $\vec{b}$ are the lattice vectors of the vdWHs. Additionally, the total energy with in-plane shift for GaS/$MoTe_2$ (WTe_2) vdWHs are listed in Figs. 1(a) and 1(b). Among them, the $A_{0,0}$ stacking pattern is thermodynamically preferred with the lattice constant of 3.594 (3.602) Å to GaS/$MoTe_2$ (WTe_2) vdWHs. The top and side views for the most stable configuration (A_{00}) of GaS/$MoTe_2$ (WTe_2) vdWHs are demonstrated in Figs.1(c) and 1(d).

The most stable interlayer distance of GaS/$MoTe_2$ (WTe_2) vdWHs is 3.212 (3.186) Å, respectively. Note that for single material, the optimized lattice constants of GaS, $MoTe_2$, and WTe_2 are also calculated, which are 3.638, 3.550, and 3.551 Å, as shown in Table S1, which agree with previous reports [52–56]. Thus, based on the unit cells of GaS, $MoTe_2$, and WTe_2, the lattice mismatch of GaS/$MoTe_2$ (WTe_2) vdWHs are 1.22 (1.24)%.

To explore the electronic characteristics of the two vdWHs, we calculate the band structures of corresponding monolayer and GaS/$MoTe_2$ (WTe_2) vdWHs (see Fig. S1 and Fig. S2 of

Supplemental Material [57]). For the HSE06 (PBE) method, the indirect band gap for GaS is 3.27 (2.37) eV, while the band gap for $MoTe_2$ and WTe_2 exhibits direct properties with values of 1.50 (1.08) eV and 1.47 (1.07) eV, which are also in accordance with existing results [52–56]. Phonon dispersion curves of WTe_2 monolayer and GaS/$MoTe_2$ (WTe_2) vdWHs are depicted in Fig. S3. All the phonon frequencies are positive, which indicates that they are dynamically stable. Then, the work function (energy-level differences between the vacuum E_{vac} and Fermi level E_f) of GaS and $MoTe_2$ (WTe_2) monolayers are calculated with the value of 6.79 and 5.15 (4.92) eV, respectively. Since the work function of monolayer GaS is larger than that of $MoTe_2$ (WTe_2), the electrons are transferred from $MoTe_2$ (WTe_2) to GaS layer when the GaS/$MoTe_2$ (WTe_2) vdWHs are constructed. Thus, the negative charges accumulate in the GaS layer and positive charges gather in the $MoTe_2$ (WTe_2) layer, and then the built-in electric field can be formed, which can induce the drift of electrons and holes and achieve balance with the diffusion force.

Interestingly, it is found that the band structures of GaS/$MoTe_2$ (WTe_2) vdWHs display the semiconducting characteristic, and the conduction-band minimum (CBM) and the valence-band maximum (VBM) of the two vdWHs are both at K point, resulting in the direct band structures. Also, the value of band gaps for GaS/$MoTe_2$ (WTe_2) vdWHs are 1.38 (1.31) eV and 0.99 (0.93) eV for the HSE06 and PBE method. As illustrated in Figs. 1(e) and 1(f), the layer-dependent projected band structures are explored in detail. The blue line and orange (red) line represent the contribution of GaS and $MoTe_2$ (WTe_2) in the GaS/$MoTe_2$ (WTe_2) vdWHs, respectively. The band alignment of vdWHs depends on the contribution of each layer to the conduction- and valence bands. Both CBM and VBM of GaS/$MoTe_2$ (WTe_2) vdWHs are offered by the $MoTe_2$ (WTe_2) material, which results in the construction of straddling band alignment. Note that the regulation method of interlayer distance remains the characteristics of straddling band alignment and direct band structures, where computation details are shown as Fig. S4 and Fig. S5. Both electrons and holes are prone to be localized inside $MoTe_2$ (WTe_2) layer and then lead to rapid recombination, which is able to apply in the luminescent aspect, such as light-emitting diodes.

B. Electric field and external biaxial strain modulation on the band structures

In general, exerting electric field and biaxial strain can play an important role to modulate electronic and optical characteristics of 2D vdWHs. Therefore, the variation of band gap and band alignment of GaS/$MoTe_2$ (WTe_2) vdWHs with the electric field and external biaxial strain are designed to study the related performance.

Firstly, Figs. 2(a) and 2(b) give the external electric-field influences on the band gap of GaS/$MoTe_2$ (WTe_2) vdWHs. Here, the external electric field is applied normal to the interface of GaS/$MoTe_2$ (WTe_2) vdWHs, and the positive direction is defined from $MoTe_2$ (WTe_2) layer to GaS layer. When the electric field from −0.50 to 0.23 (0.13) V/Å is applied to GaS/$MoTe_2$ (WTe_2) vdWHs, the direct band gap

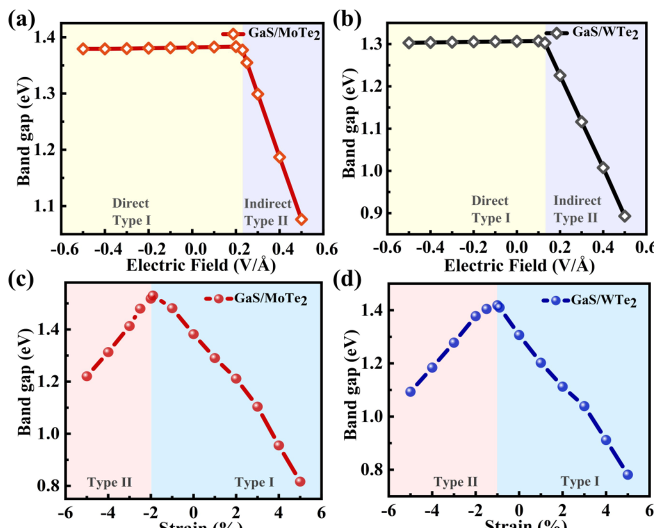

FIG. 2. Variation of the band gap of (a), (c) GaS/$MoTe_2$ and (b), (d) GaS/WTe_2 vdWHs as a function of electric fields and biaxial strains, respectively.

and type-I band alignments are maintained, and when the positive electric field increases from 0.23 (0.13) to 0.50 V/Å, the band gap demonstrates a linear decline from 1.38 (1.31) to 1.07 (0.89) eV. Interestingly, this GaS/$MoTe_2$ (WTe_2) vdWHs can also realize a transition from straddling to staggered gap. To further explore the mechanism, Fig. 3 and Fig. 4 display the electric-field influences on the electronic band structures and band alignments for the two vdWHs. As it is clearly seen, the positive electric field can make the conduction- and valence-band edges of GaS shift downward, and the CBM of $MoTe_2$ (WTe_2) moves away from the Fermi level. When the magnitude of applied electric field is further increased, the GaS contributes significantly to the CBM of the GaS/$MoTe_2$ (WTe_2) vdWHs. Thus, the transition can be realized from type-I to type-II band alignment because the value of CBM for GaS is lower than that of $MoTe_2$ (WTe_2). In addition, Fig. 3 and Fig. 4 also show that when the external electric field is applied along the negative direction, the CBM and VBM of the $MoTe_2$ (WTe_2) slide downward, while the CBM of the GaS shifts upward and VBM is scarcely changed, which implies the two vdWHs have maintained the type-I alignment.

The mechanism of tunable electronic properties of the two vdWHs under an electric field can be described as follows. An applied positive external electric field can strengthen the built-in electric field, and restrict the charge transfer from the $MoTe_2$ (WTe_2) to GaS layer. However, the charge drift induced by electric field can facilitate the charge transfer from the GaS to $MoTe_2$ (WTe_2) layer, shifting the bands of the $MoTe_2$ (WTe_2) upward and the GaS downward. Thus, the gap exhibits the declined trend. In addition, with increasing the external electric field, the CBM of GaS at M-point is lower in energy than that of the CBM at K point of $MoTe_2$ (WTe_2), turning both the vdWHs to an indirect band-gap type-II vdWH.

On the other hand, when the negative electric field is applied to the GaS/$MoTe_2$ (WTe_2) vdWHs, its direction is opposite to that of the built-in electric field, which can

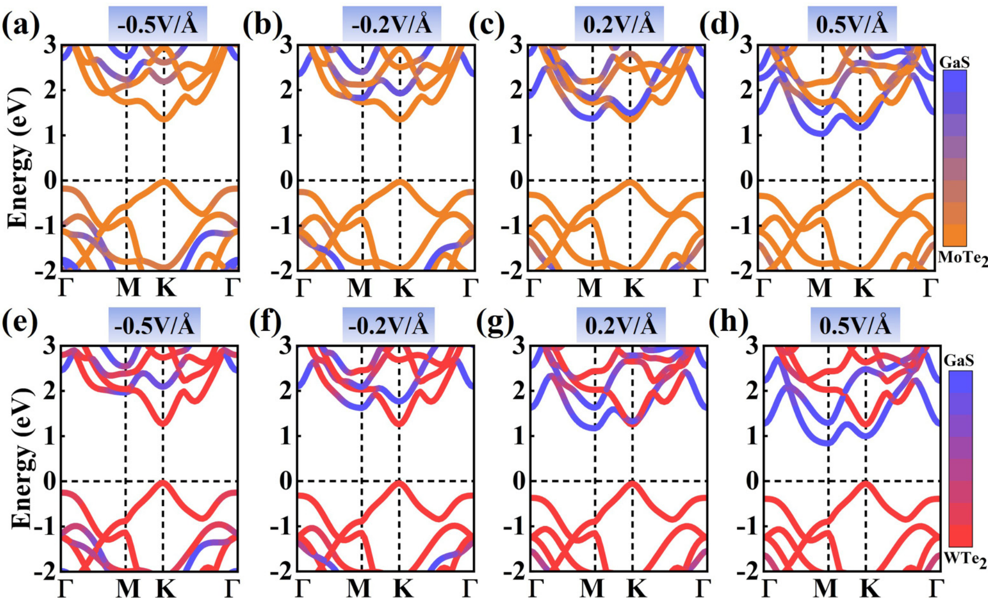

FIG. 3. Layer-dependent projected band spectra of (a)–(d) $GaS/MoTe_2$ and (e)–(h) GaS/WTe_2 vdWHs under the electric fields of −0.5, −0.2, 0.2, and 0.5 V/Å.

promote the charge from the $MoTe_2$ (WTe_2) to GaS layer, further weakening the strength of the built-in electric field. Therefore, the accumulation of electrons in the GaS layer shifts its bands upward, and the bands of $MoTe_2$ (WTe_2) move downward accordingly. Also, the detailed band structures can be observed in Fig. S6. As a result, on the application of positive electric field at $0.3 \sim 0.5$ ($0.2 \sim 0.5$) V/Å, the $GaS/MoTe_2$ (WTe_2) vdWHs can become a type-II band alignment. In such case, photogenerated electron-hole pairs can be spatially separated with electrons and holes preferably at the GaS and $MoTe_2$ (WTe_2) layers, respectively, facilitating the formation of indirect excitons and further prolonging their lifetime. In addition, we notice that the type-I to type-II band alignment transition and band-gap variation could also be obtained via controlling the external electric field in other 2D vdWHs, such as $Ca(OH)_2/\alpha$-$MoTe_2$ [56], $MoSi_2N_4$/GaN(ZnO) [58], and α-tellurene/MoS_2 vdWHs [59]. These results imply that the external electric field has affected effectively the band gap, band-edge position, and band alignment of $GaS/MoTe_2$ (WTe_2) vdWHs.

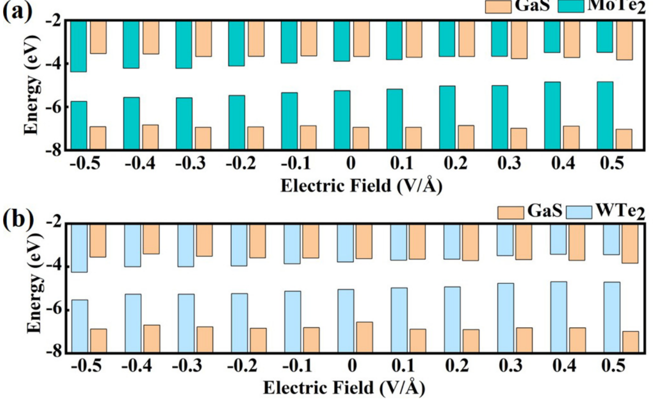

FIG. 4. Electric-field effects on the band edges of (a) $GaS/MoTe_2$ and (b) GaS/WTe_2 vdWHs.

Then, we study the biaxial strain change on the band structures of $GaS/MoTe_2$ (WTe_2) vdWHs. The strain ε is defined by $(a - a_0)/a_0$, where a and a_0 represents the lattice parameter with and without biaxial strain, respectively. Note that we use negative for compressive strain and positive for tensile strain. A strain with the change from −5 to 5% is adopted to explore the influence on electronic performance. The variations of the band gap with the strain are listed in Figs. 2(c) and 2(d). As can be seen, the increasing tensile can make the band gap exhibit a monotonously declined trend and the gap is varied from 1.38 (1.31) to 0.82 (0.69) eV, while for compressive strain, the band gap of $GaS/MoTe_2$ (WTe_2) vdWHs gradually increases and then decreases when the strain is further compressed from −2% (−1%). In particular, as shown in Table I, we take $GaS/MoTe_2$ vdWHs as an example to investigate the underlying physical mechanism for the strain effects on the electronic structures. With increasing the tensile strain for the two vdWHs, the atomic bond lengths of Mo–S, Ga–Ga, and Ga–S can be raised, while the bond angles exhibit the reduced trend. It can be obviously seen from Fig. 5 that compared with the VBM of unstrained $GaS/MoTe_2$ vdWHs, the 3% tensile strain induces the energy levels of Mo-$d_x^2 -_y^2 + d_{xy}$ orbits shift down, while that of Mo-d_z^2 is moved up to contribute mainly to the valence-band edge of strained system at the Γ point. Thus, the electronic band structures become indirect and a decreasing band gap can be observed, as shown in Fig. 6 and Fig. S8. On the other hand, with the increasing compressive strain, the Mo–S, Ga–Ga, and Ga–S bond lengths decrease, and the bond angles consequently enhance. We compare the electronic structures of unstrained $GaS/MoTe_2$ vdWHs with the one with −3% compressive strain. The bond angles are increased, and the hybridization between the Mo-$d_x^2 -_y^2 + d_{xy}$ and Te-p states are also increased in the valence-band edge. Meanwhile, the hybridization of

TABLE I. Bond lengths as a function of biaxial strain for GaS/$MoTe_2$ and GaS/WTe_2 vdWHs.

	GaS/$MoTe_2$				GaS/WTe_2			
Strain	Type	$d_{\mathrm{Mo-S}}$ (Å)	$d_{\mathrm{Ga-Ga}}$ (Å)	$d_{\mathrm{Ga-S}}$ (Å)	Type	$d_{\mathrm{W-S}}$ (Å)	$d_{\mathrm{Ga-Ga}}$ (Å)	$d_{\mathrm{Ga-S}}$ (Å)
−5%	II	2.71	2.43	2.30	II	2.71	2.43	2.31
−3%	II	2.72	2.43	2.32	II	2.72	2.44	2.32
0	I	2.74	2.44	2.35	I	2.74	2.44	2.35
3%	I	2.76	2.45	2.38	I	2.77	2.45	2.38
5%	I	2.78	2.45	2.40	I	2.78	2.45	2.40

Ga-*p*, Ga-*d*, and S-*p* orbit can be strengthened and contribute to the conduction-band edge (see Figs. 5 and 6). The direct-band characteristics can be maintained for all the compressive-strained GaS/$MoTe_2$ vdWHs, as demonstrated in detail in Fig. S7.

Moreover, the assessment of band-edge position of the GaS/$MoTe_2$ (WTe_2) vdWHs with different biaxial strains is displayed in Fig. 7. It can be seen that with tensile strain the conduction-band edge for GaS decreases slightly and the valence-band edge increases, while the CBM and VBM for the $MoTe_2$ (WTe_2) is close to the Fermi energy. Thus, both the CBM and VBM are always contributed by $MoTe_2$ (WTe_2) in tensile strain, so the GaS/$MoTe_2$ (WTe_2) vdWHs remain straddling band alignment. In addition, with increasing compressive strain, the band edges of the $MoTe_2$ (WTe_2) layer move upward significantly, while the GaS is shifted downward, resulting a transition from straddling to staggered band alignment. Then efficient separation of electrons and holes in space is realized by staggered band alignment. As in aforementioned discussion, the biaxial strain can induce the redistribution of the orbital states. Thus, the change of the orbital couplings can be one reason for altering the electronic band structures, which can directly affect the band alignment of the heterostructures. Note that similar biaxial strain effects

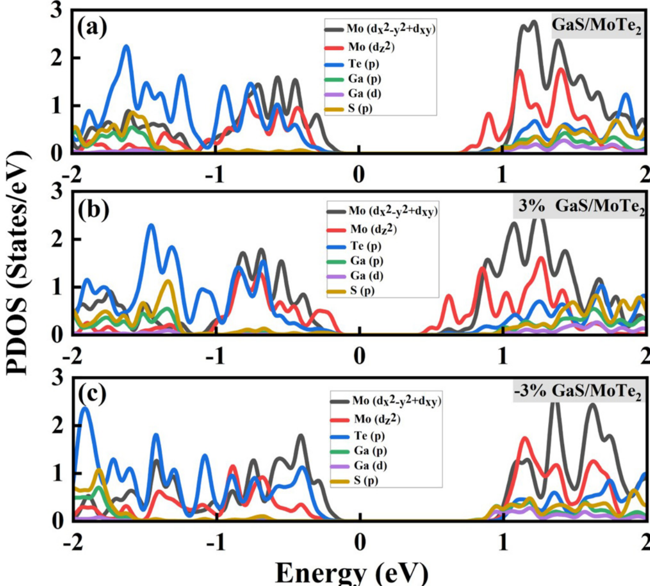

FIG. 5. Partial density of states (PDOS) of GaS/$MoTe_2$ vdWHs for (a) 0% strain, (b) 3% strain, and (c) −3% strain.

on the band structures of 2D materials-based vdWHs have been studied, such as MoSSe/MBP [30] and InSe/MoS_2 vdWHs [60]. In addition, for the electric field and strain-tuned monolayer XTe_2 (X = Mo, W) and GaS materials, previous studies also present that they can effectively change the band structures, such as band gap and direct-indirect or indirect-direct band transition [19,61–63]. However, the change of magnitude characteristics is different due to the interlayer coupling in the vdWHs.

C. Layer combination m/n modulation on the band structures

Because layer-dependent band structures are typical characteristics of 2D semiconductors, layer combination can affect the electronic structures of m-GaS/n-$MoTe_2$ (WTe_2) multilayer vdWHs, considering layer number m and n range from monolayer (1L) to five layers (5L). The corresponding band structures and the change of band alignments with the layer thickness are listed in Fig. S9 and Fig. 8.

As is observed from Fig. S9, direct structure is formed when monolayer GaS and $MoTe_2$ (WTe_2) is used to construct the GaS/$MoTe_2$ (WTe_2) bilayer vdWHs. When using few-layer GaS and $MoTe_2$ (WTe_2) to construct the GaS/$MoTe_2$ (WTe_2), however, multilayer vdWHs exhibit the characteristic of indirect band structures. Also, by changing the layer combination m/n, we can regulate the band gap of GaS/$MoTe_2$ (WTe_2) vdWHs in the range of 1.04 (0.93) to 0.71 (0.59) eV. It is notable that the band alignments of GaS/$MoTe_2$ (WTe_2) vdWHs are flexibly adjusted between straddling and staggered band alignment through varying the layer combination m/n. In addition, we can see that for the m-GaS/n-$MoTe_2$ multilayer vdWHs, when the GaS layer ($m > 2$) is larger than $MoTe_2$ layer, the type-II band alignments are presented, while for the m-GaS/n-WTe_2 multilayer vdWHs, the band structures and band alignment change are more sensitive to layer thickness regulation. This vdWHs has the straddling band alignment when the layer number of GaS is 1L ($m = 1$), and it can be transferred to staggered case with the $m > 1$.

To gain deep insight into band transition of layer combination m/n regulation, we take some representative examples of 1-GaS/5-$MoTe_2$ and 5-GaS/1-$MoTe_2$ vdWHs. In terms of 1-GaS/n-$MoTe_2$ vdWHs, as shown in Figs. 8, S9, and S10, it is clearly seen that the VBM, which originates mainly from Mo-d_Z^2 and Te-p orbitals of the $MoTe_2$ layer, is found to shift upward at the Γ point with the increasing number of $MoTe_2$ layers, resulting in the indirect band structure and a decreasing band gap. In addition, we can also observe that both the CBM and VBM are contributed by the $MoTe_2$ layer and type-I band

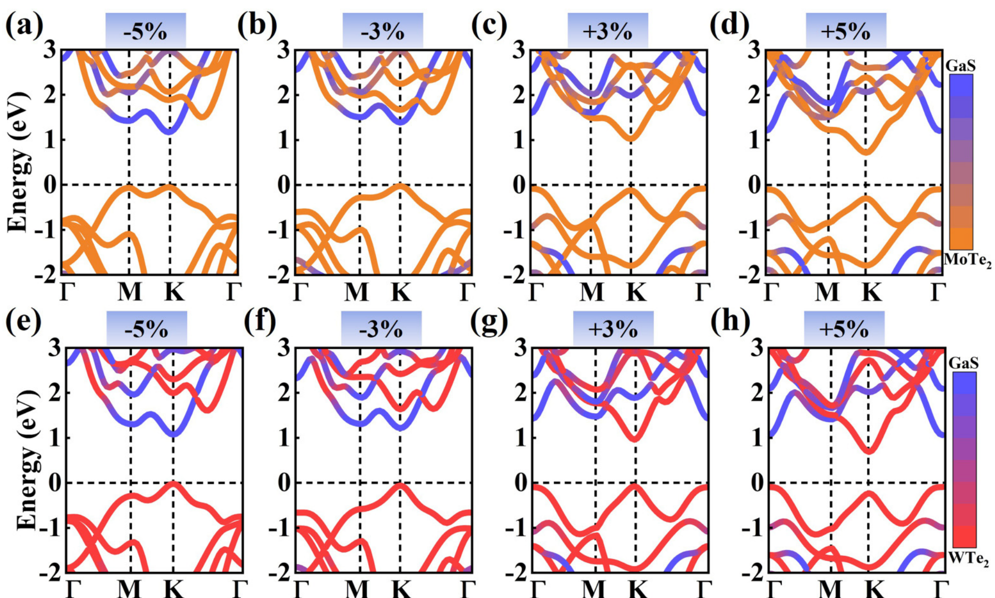

FIG. 6. Layer-dependent projected band spectra of (a)–(d) $GaS/MoTe_2$ and (e)–(h) GaS/WTe_2 vdWHs under the biaxial strains of −5, −3, 3, and 5%.

alignments are kept. Moreover, for the *m*-GaS/1-$MoTe_2$ vdWHs, when the layer number of GaS is increased, the VBM is always contributed by the Mo-$d_x^2 -_y^2 + d_{xy}$ states, whereas the hybridization of Ga-*p*, Ga-*d*, and S-*p* orbit becomes dominant to the CBM at the *M* point, and as a consequence the electronic gap exhibits indirect property. More interesting, the energy of CBM of GaS is smaller than that of $MoTe_2$, leading to a heterostructure displaying a type-II characteristics. To further shed light on the band alignment transition, we also plot the work-function difference ΔV between GaS and $MoTe_2$ freestanding monolayers with different layer numbers (see Fig. S11 of the Supplemental Material [57]). When the layer number of GaS remains unchanged, the values of ΔV are raised when the $MoTe_2$ layer number increases. On the other hand, Fig. S11 also shows that the increasing layer number of GaS induces the value of ΔV decrease when the layer thickness of $MoTe_2$ is fixed. These alterations of work-function difference can induce the charge redistribution change when forming the heterostructures. Note that for the 2D semiconductor materials, the layer number can obviously modify the band gap due to the quantum confinement effect. Thus, when the layer number combination m/n varies, the band gap and band alignment can further change in the vdWHs.

As in aforementioned investigations, for the *m*-GaS/*n*-$MoTe_2$ (WTe_2) multilayer vdWHs, with the increasing layer numbers of GaS and $MoTe_2$ (WTe_2) materials, the band edge and band structures of the vdWHs can be regulated by changing the layer combination m/n during the construction of the heterostructure, and thus the type-I and type-II band alignment transition can occur in the *m*-GaS/*n*-$MoTe_2$ (WTe_2) multilayer vdWHs. In particular, diverse types of band alignment would cause different carrier quantum confinement effects, and both are availed but possess diverse optoelectronic applications. The controllable electronic properties could offer a potential method to regulate the carrier localization in the *m*-GaS/*n*-$MoTe_2$

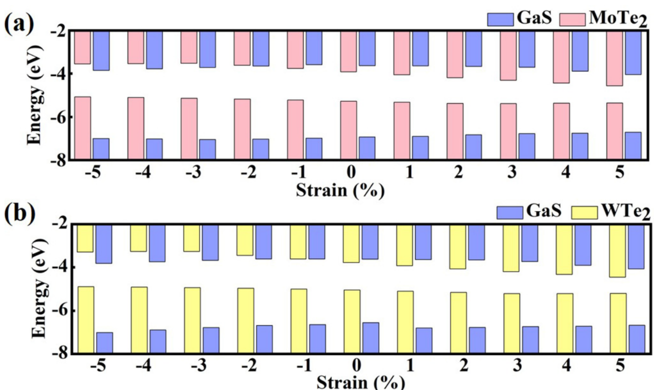

FIG. 7. Biaxial strain on the band edge of (a) $GaS/MoTe_2$ and (b) GaS/WTe_2 vdWHs.

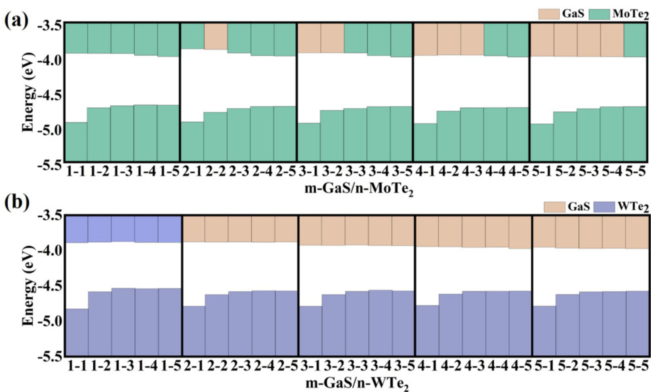

FIG. 8. Band-edge change of (a) $GaS/MoTe_2$ and (b) GaS/WTe_2 vdWHs considering different layer combinations.

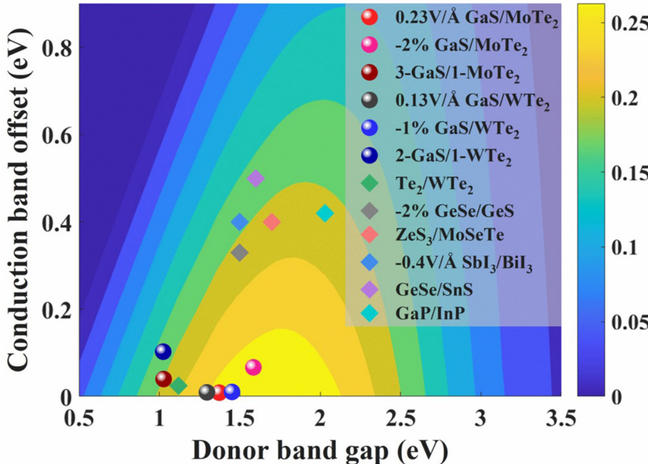

FIG. 9. Power conversion efficiencies of the GaS/$MoTe_2$ (WTe_2) vdWHs.

(WTe_2) multilayer vdWHs, which is useful to improve the performance of multifunctional devices in experiment.

D. Photoelectric applications

In this work, the change from straddling gap to staggered case has been achieved through engineering the electric field, strain, and layer combination m/n, which is favorable for the realization of high-efficiency solar cells. Thus, we estimate the PCE of the heterostructures by the method proposed by Scharber *et al.* [64], and the theoretical upper limit for PCE can be described using the following formula:

$$\eta = \frac{J_{sc}V_{oc}\beta_{FF}}{P_{\text{solar}}} = \frac{0.65\left(E_g^d - \Delta E_c - 0.3\right)\int_{E_g}^{\infty}\frac{P(\hbar w)}{\hbar w}d(\hbar w).}{\int_0^{\infty}P(\hbar w)\hbar w}. \tag{1}$$

Here, 0.65 is the band fill factor, E_g^d represents donor band gap, and ΔE_c is conduction-band offset. The $(E_g^d - \Delta E_c - 0.3)$ is the maximum open circuit voltage, where 0.3 eV is an empirical factor that has been discussed and can be taken from Ref. [64]. $P(\hbar w)$ denotes the AM 1.5 solar energy flux with $\hbar w$ of photon energy. The integrals in the numerator and denominator denote the short-circuit current and the sum of AM1.5 incident solar irradiation, respectively. E_g^d is regarded as the lower limit of integration of the term $\int_{E_g}^{\infty}\frac{P(\hbar w)}{\hbar w}d(\hbar w)$, where the electrons can be excited into a higher level after absorbing photon energy over E_g^d. Moreover, the PCE strongly depends on the conduction-band offset between the donor and acceptor layers in the heterostructure.

Suitable donor gap, small conduction-band difference, and perfect band alignment contribute to the excellent performance of PCE. In the following, Fig. 9 explores the application of PCE for high-efficiency solar cells. The PCE of GaS/$MoTe_2$ (WTe_2) bilayer vdWHs with compression strain of -2% (-1%) and 0.23 (0.13) V/Å electric field are 27.72% (28.06%) and 27.64% (26.4%), respectively. Besides, GaS/$MoTe_2$ (WTe_2) multilayer vdWHs can achieve the PCE of 20.36% (17.47%) when GaS is 3L (2L) and $MoTe_2$ (WTe_2) is monolayer. The current results are higher than the published reports, for instance, the GeSe/SnS (18%) [65], BP/SnSe (17.24% with strain) [66], ZrS3/MoSeTe (16%) [67], GaSe/GeS (16.8% with 2% strain) [68], and analogous or superlative to that of recently presented Te/$MoTe_2$ (20.1%) and Te/WTe_2 (22.5%) [69], SbI_3/BiI_3 (21.6% with electric field) [70], BAs/MoSSe (20.86%) [71], and MoS_2/BP (20.42%) [72]. Therefore, proper regulation of GaS/$MoTe_2$ (WTe_2) vdWHs paves the way for highly efficient solar cells based on the above advantages.

Moreover, to evaluate the potential application in photodetectors, we calculate the photocurrent density of m-GaS/n-$MoTe_2$ (WTe_2) multilayer vdWHs through a two-probe model operating on the photogalvanic effect. Due to the limitation of computing resources, we only select a few representative ones of these three modulations to study. As shown in Fig. 10(a), schematic construction of the presented device is demonstrated, which contains two semi-infinite electrodes (source and drain) and a central scattering region. The linearly polarized light shines perpendicularly onto the vdWHs along the x direction, and polarization of the light is parallel to the interface (in the z-y plane), which has power density of $16\,\mathrm{mW\,mm^{-2}}$. The z axis is set along the armchair direction, while the y axis is along the zigzag direction. Additionally, the photocurrent flows from the left lead to the right lead, across the scattering region (along the armchair direction). Meanwhile, the photocurrent is evoked with setting both relative permittivity and relative permeability to 1. The photocurrent originates from the separation of electron-hole pairs inside the demonstrated device with polarized light illumination. The functional relationship between photocurrent density and wavelength of visible light under different modulations is shown in Fig. 10(b).

The photocurrent density is calculated as a function of visible-light wavelength of GaS/$MoTe_2$ (WTe_2) and 2-GaS/2-$MoTe_2$ (WTe_2) vdWHs. The maximum photocurrent density is 0.77 and 1.62 $\mu\mathrm{A/mm^2}$ for the GaS/$MoTe_2$ and GaS/WTe_2 vdWHs, respectively. However, the photocurrent density of the vdWHs consisting of two bilayer components is increasing inside the visible-light range, and maximum photocurrent density can reach to 2.97 and 3.35 $\mu\mathrm{A/mm^2}$, respectively. In addition, the photoresponsivity (R_{ph}) of GaS/$MoTe_2$ (WTe_2) vdWHs and 2-GaS/2-$MoTe_2$ (WTe_2) vdWHs are 0.048 (0.101) and 0.18 (0.20) A/W, and the corresponding external quantum effect (EQE) is 8% (31%) and 42% (46%). The above results show that 2-GaS/2-$MoTe_2$ (WTe_2) vdWHs are more beneficial to enhance the characteristics of photoelectric devices. The origin of improved device performance is because of the band alignment of vdWHs transition from straddling to staggered case induced by the layer combination m/n. The regulations can make these two vdWHs get larger R_{ph} and EQE at different photon energies because the overlapped electronic states induce optical transitions in the vdWHs. Hence, the m-GaS/n-$MoTe_2$ (WTe_2) multilayer vdWHs can be taken as a prospective candidate for optoelectronic sensors.

IV. CONCLUSION

In summary, we design the GaS/$MoTe_2$ (WTe_2) multilayer vdWHs by the global structure search method to exactly

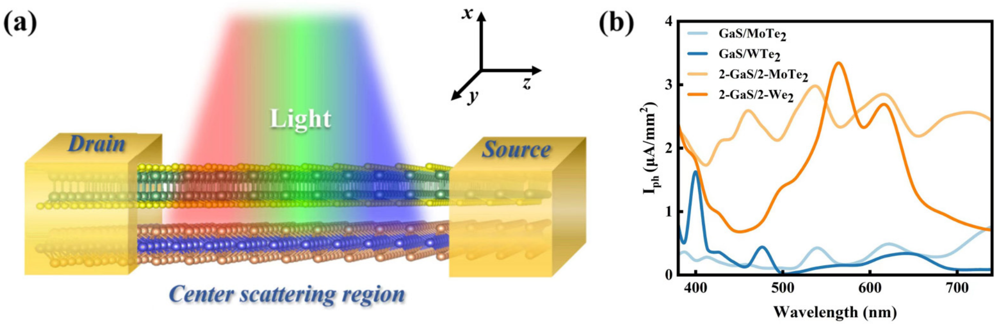

FIG. 10. Schematic diagram (a) and photocurrent density (b) of the device based on $GaS/MoTe_2$ (WTe_2) vdWHs.

explore the band structures and optical characteristics, and the engineering modulations of electric field, strain, and layer combination are considered to improve the performance of $GaS/MoTe_2$ (WTe_2) multilayer vdWHs. The vdWHs exhibit a straddling band alignment with direct band structures. With a certain compression strain and positive electric field, it can be dynamically switched from straddling gap to staggered case. The proper regulation of $GaS/MoTe_2$ (WTe_2) vdWHs can lead to a tiny conduction-band offset, staggered band alignment, and suitable donor band gap, so PCE of $GaS/MoTe_2$ (WTe_2) vdWHs with compression strain of −2% (−1%) and the electric field with 0.23 (0.13) V/Å is even up to 27.72% (28.06%) and 27.64% (26.4%), respectively. Also, $GaS/MoTe_2$ (WTe_2) multilayer vdWHs can enhance the characteristics of photodetectors, and the R_{ph} (EQE) values of $GaS/MoTe_2$ vdWHs can be increased from 0.048 (8%) to 0.18 A/W (42%). Remarkably, an excellent PCE can also be implemented by the modulation of layer combination. The results show that the 2D multilayer vdWHs can be modified for multiple function applications.

ACKNOWLEDGMENTS

This research was supported by the National Natural Science Foundation of China (Grants No. 11904085 and No. 12074103). Program for Outstanding Youth of Henan Province (Grant No. 202300410221), and Henan Innovative Science and Technology Team (Grant No. CXTD2017080). The calculations were also supported by the High Performance Computing Center of Henan Normal University.

[1] K. F. Mak, C. Lee, J. Hone, J. Shan, and T. F. Heinz, Atomically Thin MoS_2: A New Direct-Gap Semiconductor, Phys. Rev. Lett **105**, 136805 (2010).

[2] O. Kyriienko, D. N. Krizhanovskii, and I. A. Shelykh, Nonlinear Quantum Optics with Trion Polaritons in 2D Monolayers: Conventional and Unconventional Photon Blockade, Phys. Rev. Lett. **125**, 197402 (2020).

[3] H. R. Banjade, J. Pan, and Q. Yan, Monolayer 2D semiconducting tellurides for high-mobility electronics, Phys. Rev. Mater. **5**, 014005 (2021).

[4] R. Habara and K. Wakabayashi, Optically induced spin current in monolayer $NbSe_2$, Phys. Rev. B **103**, L161410 (2021).

[5] L. J. Zhou, Y. F. Zhang, and L. M. Wu, SiC_2 siligraphene and nanotubes: Novel donor materials in excitonic solar cells, Nano Lett. **13**, 5431 (2013).

[6] H. W. Guo, Z. Hu, Z. B. Liu, and J. G. Tian, Stacking of 2D materials, Adv. Funct. Mater. **31**, 2007810 (2020).

[7] C. Xia, J. Du, M. Li, X. Li, X. Zhao, T. Wang, and J. Li, Effects of Electric Field on the Electronic Structures of Broken-Gap Phosphorene/SnX_2 ($X = S$, Se) van der Waals Heterojunctions, Phys. Rev. Appl. **10**, 054064 (2018).

[8] C. Xia, W. Xiong, J. Du, T. Wang, Y. Peng, and J. Li, Universality of electronic characteristics and photocatalyst applications in the two-dimensional Janus transition metal dichalcogenides, Phys. Rev. B **98**, 165424 (2018).

[9] C. Xia, J. Du, X. Huang, W. Xiao, W. Xiong, T. Wang, Z. Wei, Y. Jia, J. Shi, and J. Li, Two-dimensional n-InSe/p-GeSe (SnS) van der Waals heterojunctions: High carrier mobility and broadband performance, Phys. Rev. B **97**, 115416 (2018).

[10] Q. Gao, X. Li, M. Li, T. Wang, X. Huang, Q. Zhang, J. Li, Y. Jia, and C. Xia, Realization of larger band gap opening of graphene and type-I band alignment with BN intercalation layer in graphene/MX_2 heterojunctions, Phys. Rev. B **100**, 115439 (2019).

[11] S. S. Lin, Z. Q. Wu, X. Q. Li, Y. J. Zhang, S. J. Zhang, P. Wang, R. Panneerselvam, and J. Li, Stable 16.2% efficient surface plasmon-enhanced graphene/GaAs heterostructure solar cell, Adv. Energy Mater **6**, 1600822 (2016).

[12] B. Zhou, A. Cui, L. Gao, K. Jiang, L. Shang, J. Zhang, Y. Li, S.-J. Gong, Z. Hu, and J. Chu, Enhancement effects of interlayer orbital hybridization in Janus MoSSe and tellurene heterostructures for photovoltaic applications, Phys. Rev. Mater. **5**, 125404 (2021).

[13] M. K. Mohanta, A. Rawat, and A. De Sarkar, Atomistic manipulation of interfacial properties in $HfN_2/MoTe_2$ van der Waals heterostructure via strain and electric field for next generation multifunctional nanodevice and energy conversion, Appl. Surf. Sci. **568**, 150928 (2021).

[14] Y. Yan, G. Abbas, F. Li, Y. Li, B. Zheng, H. Wang, and F. Liu, Self-driven high performance broadband photodetector

based on SnSe/InSe van der Waals heterojunction, Adv. Mater. Interfaces **9**, 2102068 (2022).

[15] E. Torun, H. Sahin, and F. M. Peeters, Optical properties of GaS-Ca$(OH)_2$ bilayer heterostructure, Phys. Rev. B **93**, 075111 (2016).

[16] S. Demirci, N. Avazlı, E. Durgun, and S. Cahangirov, Structural and electronic properties of monolayer group III monochalcogenides, Phys. Rev. B **95**, 115409 (2017).

[17] J. H. Lin, H. Zhang, X. L. Cheng, and Y. Miyamoto, Single-layer group IV-V and group V-IV-III-VI semiconductors: Structural stability, electronic structures, optical properties, and photocatalysis, Phys. Rev. B **96**, 035438 (2017).

[18] P. Das, D. Wickramaratne, B. Debnath, G. Yin, and R. K. Lake, Charged impurity scattering in two-dimensional materials with ring-shaped valence bands: GaS, GaSe, InS, and InSe, Phys. Rev. B **99**, 085409 (2019).

[19] A. U. Rahman, J. M. Morbec, G. Rahman, and P. Kratzer, Commensurate versus incommensurate heterostructures of group-III monochalcogenides, Phys. Rev. Mater **2**, 094002 (2018).

[20] L. A. Cipriano, G. Di Liberto, S. Tosoni, and G. Pacchioni, Quantum confinement in group III-V semiconductor 2D nanostructures, Nanoscale **12**, 17494 (2020).

[21] Y. D. Kim and J. Hone, Screen printing of 2D semiconductors, Nature (London) **544**, 167 (2017).

[22] B. Wang, A. Kuang, X. Luo, G. Wang, H. Yuan, and H. Chen, Bandgap engineering and charge separation in two-dimensional gas-based van der Waals heterostructures for photocatalytic water splitting, Appl. Surf. Sci. **439**, 374 (2018).

[23] H. T. T. Nguyen, M. M. Obeid, A. Bafekry, M. Idrees, T. V. Vu, H. V. Phuc, N. N. Hieu, L. T. Hoa, B. Amin, and C. V. Nguyen, Interfacial characteristics, Schottky contact, and optical performance of a graphene/Ga_2SSe van der Waals heterostructure: Strain engineering and electric field tunability, Phys. Rev. B **102**, 075414 (2020).

[24] J. Chen, X. He, B. Sa, J. Zhou, C. Xu, C. Wen, and Z. Sun, III-VI van der Waals heterostructures for sustainable energy related applications, Nanoscale **11**, 6431 (2019).

[25] W. Wei, Y. Dai, C. Niu, X. Li, Y. Ma, and B. Huang, Electronic properties of two-dimensional van der Waals GaS/GaSe heterostructures, J. Mater. Chem. C **3**, 11548 (2015).

[26] T. Chen, Y. Lu, Y. Sheng, Y. Shu, X. Li, R. J. Chang, H. Bhaskaran, and J. H. Warner, Ultrathin All-2D lateral graphene/gas/graphene UV photodetectors by direct CVD growth, ACS Appl. Mater. Interfaces **11**, 48172 (2019).

[27] P. Hu, L. Wang, M. Yoon, J. Zhang, W. Feng, X. Wang, Z. Wen, J. C. Idrobo, Y. Miyamoto, D. B. Geohegan *et al.*, Highly responsive ultrathin GaS nanosheet photodetectors on rigid and flexible substrates, Nano Lett. **13**, 1649 (2013).

[28] Y. Lu, T. Chen, N. Mkhize, R. J. Chang, Y. Sheng, P. Holdway, H. Bhaskaran, and J. H. Warner, GaS:WS_2 heterojunctions for ultrathin two-dimensional photodetectors with large linear dynamic range across broad wavelengths, ACS Nano **15**, 19570 (2021).

[29] B. Amin, N. Singh, and U. Schwingenschlögl, Heterostructures of transition metal dichalcogenides, Phys. Rev. B **92**, 075439 (2015).

[30] Y. Mogulkoc, R. Caglayan, and Y. O. Ciftci, Band Alignment in Monolayer Boron Phosphide with Janus MoSSe Heterobilayers under Strain and Electric Field, Phys. Rev. Appl. **16**, 024001 (2021).

[31] N. A. Pike, A. Dewandre, F. Chaltin, L. Garcia Gonzalez, S. Pillitteri, T. Ratz, and M. J. Verstraete, Spontaneous interlayer compression in commensurately stacked van der Waals heterostructures, Phys. Rev. B **103**, 235307 (2021).

[32] A. Paul and I. Grinberg, Optical Properties of MoS_2, $MoSe_2$, WS_2, and WSe_2 Under External Electric Field, Phys. Rev. Appl. **17**, 024042 (2022).

[33] S. H. Choi, H. J. Kim, B. Song, Y. I. Kim, G. Han, H. T. T. Nguyen, H. Ko, S. Boandoh, J. H. Choi, C. S. Oh *et al.*, Epitaxial single-crystal growth of transition metal dichalcogenide monolayers via the atomic sawtooth Au surface, Adv. Mater. **33**, e2006601 (2021).

[34] A. T. Hoang, K. Qu, X. Chen, and J. H. Ahn, Large-area synthesis of transition metal dichalcogenides via CVD and solution-based approaches and their device applications, Nanoscale **13**, 615 (2021).

[35] K. Liang, T. Huang, K. Yang, Y. Si, H. Wu, J. Lian, W. Huang, W. Hu, and G. Huang, Dipole Engineering of Two-Dimensional van der Waals Heterostructures for Enhanced Power-Conversion Efficiency: The Case of Janus Ga_2SeTe/InS, Phys. Rev. Appl. **16**, 054043 (2021).

[36] M. K. Mohanta, A. Arora, and A. De Sarkar, Effective modulation of ohmic contact and carrier concentration in a graphene-MgX (X = S, Se) van der Waals heterojunction with tunable band-gap opening via strain and electric field, Phys. Rev. B **104**, 165421 (2021).

[37] B. Sun, Y. Ding, P. He, Y. Zhao, and M. Cai, Tuning the Band Alignment and Electronic Properties of GaSe/SnX_2 ($X = $ S, Se) Two-Dimensional van der Waals Heterojunctions via an Electric Field, Phys. Rev. Appl. **16**, 044003 (2021).

[38] C. Q. Nguyen, Y. S. Ang, S.-T. Nguyen, N. V. Hoang, N. M. Hung, and C. V. Nguyen, Tunable type-II band alignment and electronic structure of $C_3N_4/MoSi_2N_4$ heterostructure: Interlayer coupling and electric field, Phys. Rev. B **105**, 045303 (2022).

[39] K. Zollner, P. E. F. Junior, and J. Fabian, Strain-tunable orbital, spin-orbit, and optical properties of monolayer transition-metal dichalcogenides, Phys. Rev. B **100**, 195126 (2019).

[40] N. Shehzad, I. Shahid, S. Yao, S. Ahmad, A. Ali, L. Zhang, and Z. Zhou, A first-principles study of electronic structure and photocatalytic performance of two-dimensional van der Waals MTe_2-As (M = Mo, W) heterostructures, Int. J. Hydrogen. Energy **45**, 27089 (2020).

[41] G. Kresse and J. Furthmuller, Efficient iterative schemes for ab initio total-energy calculations using a plane-wave basis set, Phys. Rev. B **54**, 11169 (1996).

[42] G. Kresse and J. Hafner, Ab initio molecular dynamics for liquid metals, Phys. Rev. B **47**, 558 (1993).

[43] G. Kresse and J. Hafner, Ab initio molecular-dynamics simulation of the liquid-metal-amorphous-semiconductor transition in germanium, Phys. Rev. B **49**, 14251 (1994).

[44] J. P. Perdew, K. Burke, and M. Ernzerhof, Generalized Gradient Approximation Made Simple, Phys. Rev. Lett **77**, 3865 (1996).

[45] P. E. Blöchl, Projector augmented-wave method, Phys. Rev. B **50**, 17953 (1994).

[46] J. Heyd, G. E. Scuseria, and M. Ernzerhof, Hybrid functionals based on a screened Coulomb potential, J. Chem. Phys. **118**, 8207 (2003).

[47] G. Kresse and D. Joubert, From ultrasoft pseudopotentials to the projector augmented-wave method, Phys. Rev. B **59**, 1758 (1999).

[48] S. Grimme, Semiempirical GGA-type density functional constructed with a long-range dispersion correction, J. Comput. Chem. **27**, 1787 (2006).

[49] T. Kerber, M. Sierka, and J. Sauer, Application of semiempirical long-range dispersion corrections to periodic systems in density functional theory, J. Comput. Chem. **29**, 2088 (2008).

[50] H. J. Monkhorst and J. D. Pack, Special points for Brillouin-zone integrations, Phys. Rev. B **13**, 5188 (1976).

[51] S. Smidstrup, T. Markussen, P. Vancraeyveld, J. Wellendorff, J. Schneider, T. Gunst, B. Verstichel, D. Stradi, P. A. Khomyakov, U. G. Vej-Hansen *et al.*, QuantumATK: An integrated platform of electronic and atomic-scale modelling tools, J. Phys.: Condens. Matter **32**, 015901 (2020).

[52] M. J. Szary, M. T. Michalewicz, and M. W. Radny, Bonding and electronics of the $MoTe_2$/Ge interface under strain, Phys. Rev. B **95**, 205421 (2017).

[53] M. G. Menezes and S. Ullah, Unveiling the multilevel structure of midgap states in Sb-doped MoX_2 (X = S, Se, Te) monolayers, Phys. Rev. B **104**, 125438 (2021).

[54] M. Pisarra, C. Díaz, and F. Martín, Theoretical study of structural and electronic properties of 2H-phase transition metal dichalcogenides, Phys. Rev. B **103**, 195416 (2021).

[55] H. Zhao, E. Li, C. Liu, Y. Shen, P. Shen, Z. Cui, and D. Ma, DFT computation of two-dimensional CdO/GaS van der Waals heterostructure: Tunable absorption spectra for water splitting application, Vacuum **192**, 110434 (2021).

[56] Q. Gao, C. Xia, W. Xiong, J. Du, T. Wang, Z. Wei, and J. Li, Type-I $Ca(OH)_2/\alpha$-$MoTe_2$ vdW heterostructure for ultraviolet optoelectronic device applications: Electric field effects, J. Mater. Chem. C **5**, 12629 (2017).

[57] See Supplemental Material at http://link.aps.org/supplemental/10.1103/PhysRevB.106.125306 for the band structures of GaS, $MoTe_2$, and WTe_2 monolayers, the projected band structures of GaS/$MoTe_2$ and GaS/WTe_2 vdWHs with different interlayer distances, electric fields, biaxial strains, layer thickness, and the work-function difference.

[58] J. Q. Ng, Q. Wu, L. K. Ang, and Y. S. Ang, Tunable electronic properties and band alignments of $MoSi_2N_4$/GaN and $MoSi_2N_4$/ZnO van der Waals heterostructures, Appl. Phys. Lett. **120**, 103101 (2022).

[59] W. Zhang, D. Chang, Q. Gao, C. Niu, C. Li, F. Wang, X. Huang, C. Xia, and Y. Jia, Interlayer coupling and external electric field tunable electronic properties of a 2D type-I α-tellurene/MoS_2 heterostructure, J. Mater. Chem. C **6**, 10256 (2018).

[60] R. Sen, K. Jatkar, and P. Johari, Modulation of electronic and transport properties of bilayer heterostructures: InSe/MoS_2 and InSe/h-BN as the prototype, Phys. Rev. B **101**, 235425 (2020).

[61] W. S. Yun, S. W. Han, S. C. Hong, I. G. Kim, and J. D. Lee, Thickness and strain effects on electronic structures of transition metal dichalcogenides: 2H-MX_2 semiconductors (M = Mo, W;X = S, Se, Te), Phys. Rev. B **85**, 033305 (2012).

[62] M. Yagmurcukardes, R. T. Senger, F. M. Peeters, and H. Sahin, Mechanical properties of monolayer GaS and gase crystals, Phys. Rev. B **94**, 245407 (2016).

[63] I. Ahmad, S. A. Khan, M. Idrees, M. Haneef, I. Shahid, H. U. Din, S. A. Khan, and B. Amin, Influence of strain on specific features of MoX_2 (X = S, Se, Te) monolayers, Physica B **545**, 113 (2018).

[64] M. C. Scharber, D. Mühlbacher, M. Koppe, P. Denk, C. Waldauf, A. J. Heeger, and C. J. Brabec, Design rules for donors in bulk-heterojunction solar cells—towards 10% energy-conversion efficiency, Adv. Mater **18**, 789 (2006).

[65] X. Lv, W. Wei, C. Mu, B. Huang, and Y. Dai, Two-dimensional GeSe for high performance thin-film solar cells, J. Mater. Chem. A **6**, 5032 (2018).

[66] W. Dou, A. Huang, Y. Ji, X. Yang, Y. Xin, H. Shi, M. Wang, Z. Xiao, M. Zhou, and P. K. Chu, Strain-enhanced power conversion efficiency of a BP/SnSe van der Waals heterostructure, Phys. Chem. Chem. Phys **22**, 14787 (2020).

[67] R. Ahammed, A. Rawat, N. Jena, Dimple, M. K. Mohanta, and A. De Sarkar, ZrS_3/MS_2 and ZrS_3/MXY (M = Mo, W; X, y = S, Se, Te; x ≠ Y) type-II van der Waals hetero-bilayers: Prospective candidates in 2D excitonic solar cells, Appl. Surf. Sci **499**, 143894 (2020).

[68] B. Zhou, S.-J. Gong, K. Jiang, L. Xu, L. Shang, J. Zhang, Z. Hu, and J. Chu, A type-II GaSe/GeS heterobilayer with strain enhanced photovoltaic properties and external electric field effects, J. Mater. Chem. C **8**, 89 (2020).

[69] K. Wu, H. Ma, Y. Gao, W. Hu, and J. Yang, Highly-efficient heterojunction solar cells based on two-dimensional tellurene and transition metal dichalcogenides, J. Mater. Chem. A **7**, 7430 (2019).

[70] K. Lai, H. Li, Y. K. Xu, W. B. Zhang, and J. Dai, Achieving a direct band gap and high power conversion efficiency in an SbI_3/BiI_3 type-II vdW heterostructure via interlayer compression and electric field application, Phys. Chem. Chem. Phys. **21**, 2619 (2019).

[71] M. K. Mohanta and A. De Sarkar, Interfacial hybridization of Janus MoSSe and BX (X = P, As) monolayers for ultrathin excitonic solar cells, nanopiezotronics and low-power memory devices, Nanoscale **12**, 22645 (2020).

[72] M. K. Mohanta, A. Rawat, N. Jena, R. Ahammed Dimple, and A. De Sarkar, Interfacing boron monophosphide with molybdenum disulfide for an ultrahigh performance in thermoelectrics, two-dimensional excitonic solar cells, and nanopiezotronics, ACS Appl. Mater. Interfaces **12**, 3114 (2020).